Lightwave-driven electron emission for polarity-sensitive terahertz beam profiling

Simon Jappe Lange[1*], Matthias C. Hoffmann[2] and Peter Uhd Jepsen[1*]

[1]Department of Electrical and Photonics Engineering, Technical University of Denmark, DK-2800 Kongens Lyngby, Denmark

[2]Linac Coherent Light Source, SLAC National Accelerator Laboratory, 2575 Sand Hill Road, Menlo Park, CA 94025, USA

*Authors to whom correspondence should be addressed: slla@dtu.dk, puje@dtu.dk .

Abstract: Full exploitation of advanced light sources in the terahertz (THz) frequency range requires versatile experimental tools to fully characterize the spatial, temporal, and spectral shape of the THz electric field. Several techniques for passive THz beam profiling exist that offer information about the temporally integrated intensity. Thus, any information about the electric field itself is lost. Here we show that UV-visible light emission produced via lightwave-driven field emission from single-layer metasurfaces can be used to visualize the peak electric field distribution of THz beams in real time. Our technique is scalable up to frequencies approaching the plasma frequency of the metal used for the metasurface. Uniquely, our device is sensitive to the absolute polarity of the THz lightwave. These findings demonstrate a general pathway to designing meta-material-based field-sensitive optical detectors suitable for the entire THz and IR spectral region.

I. Introduction

Generation and detection of electromagnetic radiation in the terahertz (THz) frequency range are key enabling technologies for investigation of a wealth of light-matter interactions [1-7] as well as for material characterization, spanning from fundamental elements over electronic circuits, cancer cells, artisanal artwork and explosives, among others [8-12]. THz source technology has matured tremendously over the past decades, enabling intense, coherent single-cycle THz pulses across the entire far-infrared from table-top systems as well as accelerator-based THz sources with very high average power and spectral coverage [13, 14]. With the increasing pace of research and emerging applications in the THz range, the rapid profiling of more than the basic transverse intensity profile of THz beams is becoming more and more relevant. A large class of THz sources deliver quasi-single-cycle pulses with a very large bandwidth, where the peak electric field and its absolute polarity plays a key role in the understanding of physical processes such as THz generation from laser-driven plasmas [15, 16], field-driven electron emission [17-19], high harmonic generation [20, 21], and

nonlinear semiconductor dynamics [22]. These examples represent different manifestations of lightwave electronics [23], where the instantaneous electric (or magnetic) field of the optical waveform determines the physics of the interaction between light and matter on a sub-cycle time scale [24]. The temporal shape of the electric field $E(t)$ can be characterized by photoconductive sampling [25], free-space electro-optic sampling [26] and air biased coherent detection [15, 27], techniques which all rely on heterodyne optical sampling with a synchronous femtosecond laser pulse with at least the same bandwidth as the THz field [1]. The complete spatial profile $E(x, y, z, t)$ can be characterized by similar techniques, by raster scanning of a single-point detector [1] or electro-optic sampling using a large-area detection crystal [28], again with an ultrafast synchronized gate signal. Incoherent imaging with THz illumination from molecular gas lasers was described early on [29], and today beam profiling techniques for long wavelengths include pyroelectric [30], VO_x microbolometer [31, 32] and thermopile [33] focal plane arrays (FPAs). All these incoherent methods measure the absorbed heat and are therefore sensitive only to the temporally integrated intensity of a THz beam without providing direct information about its field strength, polarization or polarity.

Here we demonstrate how electrons driven by THz-induced field emission from an array of sub-wavelength antenna structures can excite and ionize surrounding argon (Ar) gas [34] and use the resulting glow discharge to map the cross-sectional peak electric field distribution of THz field transients. We discuss the optimized design of the antenna structures, and then characterize the field dependence of the Ar glow discharge and compare it to predictions by standard electron tunneling (Fowler-Nordheim) theory. We demonstrate that by designing the antenna structure in an asymmetric manner, it is possible to determine the absolute polarity of an asymmetric quasi-single-cycle THz-frequency lightwave. Finally, arrangement of the antenna structures in an array enables imaging of the transverse profile of a focused THz beam, and we demonstrate this capability and the applications enabled by the strong nonlinearity of the emission process compared to conventional microbolometer imaging arrays.

II. Device design and simulation results

A. General principles

An experimentally recorded image is shown in Figure 1f, and the basic concept is illustrated in Figure 1a and Figure 1e. Here, THz single-cycle pulses are focused from the back side of a 525 µm-thick high-resistivity Si (HR-Si) substrate with 1 µm SiO_2 thermally grown on top [35]. On top of the oxide layer, antenna structures (Ti/Au, 10/200 nm) concentrate the field in a small central region. An SEM micrograph of the resulting antennas is found in Figure 1b. The electric near-field at the metallic edges thereby reaches values >2 orders of magnitude larger than that of the incident peak electric THz field (Figure 1c and Figure 1d), which drives a field emission tunnel current J_{FN} from the antenna tips into free space according to the highly nonlinear Fowler-Nordheim (FN) equation

$$J_{FN} = a_{FN}\frac{(\beta F)^2}{\Phi}\exp\left(-\frac{b_{FN}\Phi^{\frac{3}{2}}}{\beta F}\right),$$

where F is the externally applied electric field, β is the field enhancement factor at the emitter-vacuum interface, Φ is the emitter material work function and a_{FN}, b_{FN} are the FN constants [36]. The emitted electrons subsequently undergo sub-cycle lightwave acceleration in the strong nearfield and may eventually collide with and excite nearby argon (Ar) atoms, hereby creating a local microplasma with a glow discharge that is recorded with a standard CMOS camera. The Ar plasma glow discharge spectrum primarily reside in the near-IR and red, where Si-based cameras are very sensitive [37, 38].

It has previously been demonstrated how metal-based metasurfaces can be used to visualize the electric field of high-power THz transients by means of field enhancement and subsequent nonlinear effects like field emission, electromigration, material breakdown and THz-induced photoluminescence [4, 39, 40]. It has also been demonstrated how a plasma discharge can be used for THz detection, although without any metasurface implementation [41] .

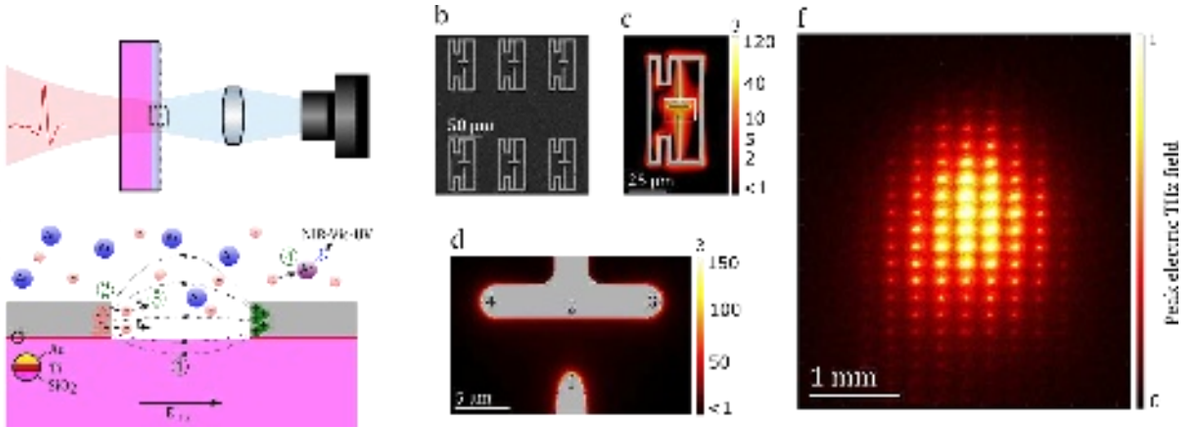

Figure 1: **THz profiling technique.** (a) An incident THz beam is focused onto gold (Au) micro-antenna structures through a Si/SiO_2 substrate. Electrons are field-emitted from the antennas and create a local argon (Ar) plasma in the vicinity their emission points. The light from the plasma glow discharge is imaged onto a CMOS sensor to record a 2D image of the emission area. (b) SEM micrograph of the micro-antenna array, corresponding to the rectangular mark-up on (a). Antennas are arranged in a periodic array with unit cell spacing $(x, y) = (74, 148)$ µm. (c) Finite-element simulation of the local electric field distribution around an antenna using a broadband THz pulse as the source. The electric field is concentrated in the central asymmetric gap of the antenna. (d) Close-up of the field distribution in the gap on a linear scale, which shows that the field enhancement is largest around the antenna-air tip interfaces and hence asymmetric. The color scale in (c) and (d) indicates the local field enhancement factor β. (e) Schematic of the THz-driven electron emission. The structure is excited by a THz field pointing to the right. The strong THz-induced local field (1) drives tunneling of electrons from the air-metal interface (2) and subsequent acceleration (3). Collision with and excitation/recombination of Ar atoms (4) is accompanied by emission of primarily visible/near-IR light which can be detected by a standard CMOS sensor. (f) An experimentally obtained transverse mode profile of a THz beam visualized by the intensity distribution of the Ar emission. This emission intensity scales with the peak electric field in a nonlinear fashion according to the Fowler-Nordheim law.

THz-driven field emission by tunneling can be a very effective process to liberate electrons. The effect can occur on a time scale shorter than the oscillation cycle of the THz field, and was demonstrated from the tips of dipole antennas [42] and across the narrow gap in split-gap dipole antennas [43]. The effect has been used for ultrafast control of tunnel currents from nanostructures in STM [3, 18, 44] and on 2D surfaces [45]. The incident electric field can be lifted into the field emission regime at MV/cm field strengths using metasurfaces with arrays of down-scaled, generic resonant structures adapted from microwave research [46-48]. Moreover, the emitted electrons can, if accelerated to sufficient kinetic energy, be used for collision-induced excitation of gas molecules surrounding the metasurface [17] that, depending of the gas species, then leads to light emission in the UV, visible and near-infrared regions. The functionality of such structures relies on the high electrical conductivity of metals such as gold (Au) that is used here. The high AC conductivity of metals spans well into the mid-IR regime, and the field enhancement factor β depends only weakly on the conductivity of the metal (see Supplementary Information) and the process is therefore scalable in frequency up to at least 100 THz.

B. Antenna simulations

To enhance the field-emission process, we designed an array of sub-wavelength antenna structures optimized for interaction with a broadband THz single-cycle transient with bandwidth between 0.1 and 1.2 THz. The design and simulations were performed with CST Microwave Studio (MWS) and CST Particle Studio (PS). If we define a field emission threshold as the field strength required to emit a single electron during the duration of the THz pulse (1 ps) from a representative area of 1 $\mu\mathrm{m}^2$, we find this threshold field to be approx. $5 \cdot 10^8$ V/m. Therefore a doubly resonant antenna structure was realized that gave the highest possible peak electric field response of the incoming THz transient in both time and space. This meant that design considerations in CST MWS relied on size- and geometry sweeps over a range of well-known antenna structures from the microwave regime.

All simulations were performed in the time domain based on a hexahedral mesh. In volumes around the electron emission points at the antenna tips, the mesh was set to $40 \times 40 \times 40$ nm. When moving away from the emission points, mesh cells were allowed to expand with up to 20% compared to their nearest neighbors. This resulted in a large cell asymmetry in volumes of less field variation. The largest mesh cell had at least one side that was 3.79 µm long, which was close to 100 times the smallest mesh cell. The incident electromagnetic field was treated as a linearly polarized plane wave and boundary conditions were periodic.

All simulations assumed linear material response to keep the computational burden to a realistic level. Any nonlinear effect in Au on a ps timescale is insignificant as it was experimentally verified with an imaging IR thermometer that metal heating was below 1°C in the strong THz field. The antenna design can be considered as two current loops driven by the same voltage bias, which is the incoming THz transient. The small loop is

first optimized for a maximum peak field enhancement a few nm from the I-shaped tip by varying width/height ratio. Afterwards, the big current loop is introduced, and the width is varied until maximum peak field enhancement is again obtained. Lastly, the big loop is "folded in" until significant cross-talk between antenna parts start to decrease the peak field enhancement again.

After CST MWS optimization, CST PS was used to introduce electron field emission and perform spatial and temporal mapping of emitted electrons using the Lorentz force law. An animated rendering of the emission under vacuum conditions can be found in Supplementary Multimedia 1. In the simulations, space charge effects are included. The color scale indicates the electron energy. Each particle in the simulation represents a charge density, which is not necessarily equal to one electron.

The structure consists of two coupled split-ring resonators of different circumference and a common gap surrounded by a flat and a pointed electrode, which we shall refer to as the T- and I-tip, respectively. Each ring constitutes a current pathway, and for a circumference ratio of 3/2, both pathways give the capacitor-like tip arrangement its maximum charge accumulation and hence field enhancement due to the peak THz electric field at the same point in time and space (Figure 2a and Figure 2b). In other words, the antenna structure is multi-resonant with its major resonance components being approximately in phase during the first 4-5 ps of interaction. Since the electron emission process is highly nonlinear and due to radiative losses, the initial time window of 4-5 ps following the interaction with the THz pulse is the only regime of interest. Our antennas are designed accordingly with a field enhancement performance that quickly degrades after 5 ps. Since J is a highly non-linear function in E, and the electric field response of the antenna quickly dies out after THz excitation, it will consequently be mainly the peak electric field strength of the incident THz transient that determines the number of emitted electrons. Therefore, our metasurface can be used for visualization of the peak electric field.

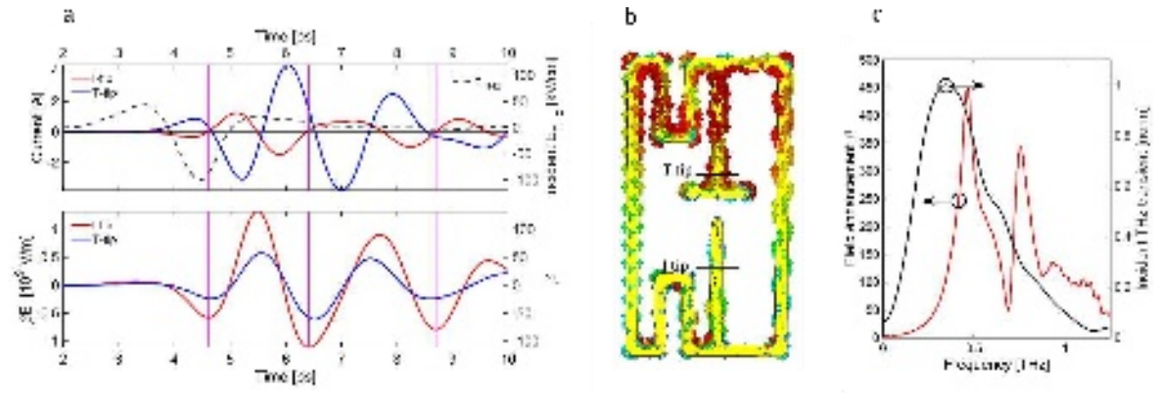

Figure 2: **Simulations of currents and electric field enhancement at the antenna.** (a) Top: a single cycle THz pulse (gray, dashed curve) with peak electric field of 100 kV/cm induces currents towards the I-tip and T-tip, which are recorded through the two cross-sections indicated in (b). The approximate zero-points of both currents coincide with the electric field enhancement β (bottom plot). This indicates a resonant enhancement of most of the frequencies included in the single-cycle pulse. (b) Surface current map at 6.4 ps, where β assumes its global maximum. The current flow to the tips

is close to zero, which is indicated as small and sparse arrows. Larger current magnitudes are indicated by bigger and more densely packed arrows. The illustration is on a linear scale. The I-tip and T-tip cross-sections are chosen such that the distance to their respective I- and T-tips is equal. (c) Electric field enhancement spectrum at the I-tip (red), which shows a broadband enhancement over the spectral content of the incident THz pulse from 0.1 to 1.2 THz. The spectrum of a typical THz pulse used in the experiments (black) is shown for comparison with the field enhancement spectrum.

In the top plot of Figure 2a, we show a single cycle THz pulse with a waveform determined in experiment (gray, dashed curve) with peak electric field of -100 kV/cm along with the simulated electrical currents that it induces in the antenna through the two cross-sections shown in Figure 2b. In the bottom plot, the electric field enhancement β and the corresponding electric field is depicted as recorded 5 nm away from the antenna-vacuum interface above the I-tip and below the T-tip. The approximate location of the two points is indicated on Figure 1d. We see that the local, enhanced electric field is oscillating out of phase with respect to the incident electric field, and that the temporal shape of the local field is significantly different from that of the incident field due to the frequency-dependent field enhancement factor. The maximum field enhancement in time for the used THz pulse is $\beta = 132$. The purple, vertical lines on Figure 2a indicate the three most pronounced peaks in the electric field at a field polarity that enables only electron emission from the I-tip. By following these lines to the top plot, one can see that they closely correspond to situations where the current flow to the two tips is zero. This situation is indicative of a resonant antenna behavior where the largest field enhancement on the tip corresponds to that where the capacitive-like gap is charged with its maximum electric charge.

In Figure 2b, an image of the surface current distribution at 6.4 ps, where the electric field enhancement assumes its global maximum, is shown. Not only can it be seen that the current flow to the tips is close to zero; it is also apparent that there is a complicated current flow with multiple nodes around the entire antenna structure, which would not be the case for a single resonant antenna like an electric dipole. This flow originates from the beating between the two main resonances pertaining to the two rings, which collectively make up a broad enhancement spectrum at the I-tip as shown in Figure 2c. The spectrum is obtained from the Fourier transform of a 30 ps long time domain simulation where the evanescent ringing originating from the resonant behavior has died out. This particular antenna is suitable for short THz laser pulses with bandwidth between 0.1 and 1.2 THz. However, by simple geometrical scaling, this enhancement spectrum can be moved to other parts of the infrared frequency spectrum since noble metals – like Au – maintain excellent electrical conductivity properties all the way up into the near-IR range. This is supported by simulations described in the Supplementary material.

III. Experimental section

A. Sample fabrication and assembly

The metasurface sample was made by growing a 1 µm thick thermal oxide on top and back of a standard 525 µm high-resistivity silicon wafer (HR-Si) with an electrical resistivity greater than 10^4 Ωcm. The uniformity

and exact thickness of the layer was not crucial and therefore not thoroughly investigated. Subsequently, a periodic antenna array was patterned using standard UV photolithography using a mask with 1.5 µm tolerance and a resist with positive polarity. The antennas were designed to be 3 µm wide.

We placed the array on a SiO_2 buffer layer to suppress nonlinear electrical breakdown effects in the silicon substrate due to the antenna nearfields, which reach strengths more than 2 orders of magnitude above their DC breakdown values. We have found experimentally that placing antennas directly on HR-Si leads to reduced light emission and degradation of the metasurface in a matter of minutes, owing to current paths in the substrate due to impact ionization and irreversible modifications of the HR-Si induced by the strong electric field [19, 35].

The SEM micrograph in Figure 3 shows that a soft tapering of tips was nicely obtained. 10 nm Ti and 200 nm Au was deposited using electron beam evaporation. The Ti layer was used for better Au adhesion to the substrate. Lift-off was performed in N-Methyl-Pyrrolidone. The sample was cut at 10×10 mm. The antenna spacing was $(x, y) = (74, 148)$ µm, thus a sample held $135 \times 67 = 9045$ antennas optimized for a response between 0.1 and 1.2THz.

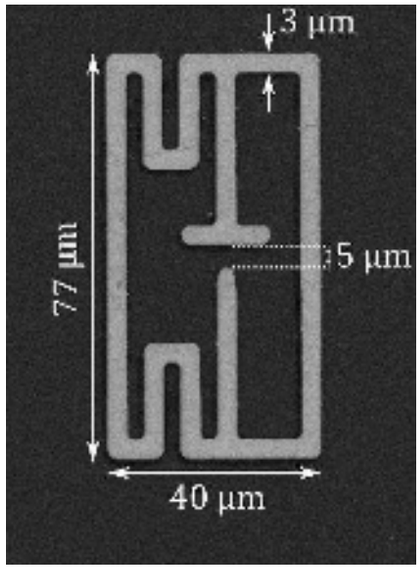

Figure 3: SEM micrograph showing one antenna with its important spatial dimensions in top view.

The metasurface was placed as a sidewall in a small pressure control chamber with antennas pointing inwards. The THz pulse was incident at normal incidence from the back, thus suffering from a 30% Fresnel reflection loss. Electron field emission and plasma generation was realized by introducing argon (Ar) gas in the chamber at variable pressure. The glow discharge light was imaged through a back window with a 20x microscope lens. The camera had a monochrome 2.8 megapixel CCD sensor (Lumenera Infinity 3-3URM).

B. THz pulse generation and detection

We used a 3.4 W, 110 fs Ti:Sapphire regeneratively amplified laser (SpectraPhysics Spitfire Ace) with a central wavelength of 800 nm for THz generation and detection. The repetition rate was 1 kHz. Quasi-single-cycle THz pulses were generated by optical rectification in $LiNbO_3$ crystal using the tilted pulse front excitation scheme [49, 50]. The THz pulses have energies of a few μJ and bandwidth from 0.1 to 1.2 THz, with a maximum at 0.5 THz. Free-space electro-optic (EO) sampling [51, 52] with a 1-mm (110) ZnTe crystal was used to acquire THz time traces and estimate the peak electric field. THz beam profiling was performed in the THz focus by exchanging the ZnTe crystal with the metasurface imaging system or a microbolometer array (NEC, model IRV-T0831).

C. Experimental demonstration of polarity sensitivity

Depending on the relative orientation of the asymmetric gap to the incident peak field polarity, the maximum charge accumulation will happen either at the T- or I-tip. The strength and spatial distribution of the field emission associated with the charge accumulation will therefore depend on the incident field polarity, as discussed below and shown in Figure 4. Consequently, we can distinguish between different polarities with an array of antennas of alternating orientation.

Metasurfaces that aim to enhance the incident electric field significantly can benefit from field coupling between the individual surface elements [46, 53]. However, for a beam profiling device, elements with such non-local coupling would give an image where the imaged electric field at each pixel depended on the electric field distribution on the entire surface. Our antenna element is therefore designed to encapsulate the field enhancement inside the antenna itself to avoid significant coupling with neighboring antennas (Figure 1d). Simulations (not shown) confirm that the local field enhancement is independent of the lattice spacing of the resonant structures when placed in an array. As a result, the light intensity from an arbitrary pixel can be interpreted as a measure of the electric field at the closest emission point. The decoupling of elements also makes it feasible to pack the individual antennas closely for increased resolution. For further miniaturization, the current pathway in the largest split-ring is folded in bends to minimize its area (Figure 1b and Figure 1c).

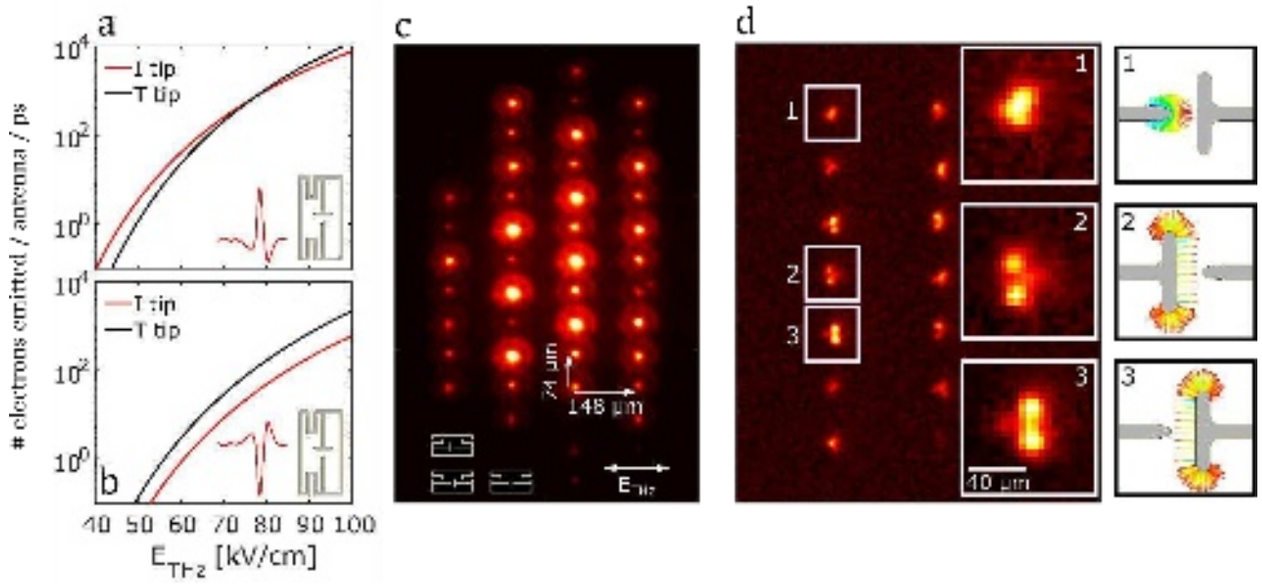

Figure 4: **Polarity determination.** (a,b) Simulated electron emission from the I- and T-tips of an antenna in two opposite orientations as function of peak incident THz field. Electron emission from the T-tip includes both the flat side oriented towards the I-tip as well as the two end tips – all three sides are shown in Figure 1d. In the top configuration, the field enhancement at the I-tip is larger than at the T-tip, but the total emission area is larger on the latter. As a result, the main electron emission shifts from the I-tip to the T-tip with increasing field strength. In the bottom configuration (opposite polarity of the THz pulse) the field enhancement on the T-tip is largest, so no such cross-over situation occurs. The total electron emission is largest in the top configuration. (c) Experimental result from illumination of an antenna array with alternating antenna orientations. Antennas with one orientation clearly emit more light than the other. The brightest light comes from the antenna-field configuration in (a). (d) Optimized experiment to resolve the actual electron emission points. The total light intensity is higher in situation 3 compared to 2, suggesting that the former is the antenna-field configuration in (a). The antenna orientation is the same in situations 1 and 3. The former sits in a lower field than the latter and the main electron emission shifts from the T-tip to the I-tip, in line with the earlier polarity observation. In the right panels, simulated electron emission maps are illustrated for the three cases. Blue colors indicate low kinetic energy, while red colors indicate higher energy on a linear scale.

In Figure 4, we show the capability of the metasurface to be used for absolute polarity determination in two different ways. The insets in Figure 4a and Figure 4b illustrate two different simulated cases where an antenna is illuminated with a single cycle pulse of opposite polarities. In the top configuration, the highest field enhancement for the antenna overall occurs at the I-tip and the electron emission will therefore initiate here at low field strengths. However, when increasing the field strength, an additional emission from the T-tip starts to grow. Since the total emission area at the T-tip is constituted of two tips and a long, flat side (points 2, 3 and 4 in the Fig. 1d), its total emission increases faster than that at the I-tip. Therefore, even at lower field strengths at all emission surfaces compared to the I-tip, the T-tip emission surpasses that of the I-tip at some field strength. With the opposite polarity, the field enhancement at the T-tip is always larger than at the I-tip. Therefore, there will be no cross-over of main emission point from I-tip to T-tip. Thus, by illuminating an antenna with a well-known orientation, one can in principle determine the absolute polarity by observing whether this cross-over happens.

We observe that the total emission strength is significantly different in the two configurations, which can similarly be used for absolute polarity determination. In Figure 4c, the latter method has been used by creating an antenna array with antennas assuming alternating orientations. One particular orientation dominates over

the other in terms of total electron emission. In this case, by lowering the integration time on the CMOS camera, one obtains an image like that in Figure 4d. Three situations have been highlighted here. Situations 2 and 3 come from oppositely oriented antennas at the center of the THz beam with high electric field strength. The main light emission in both situations come from the T-tip, with situation 3 being slightly brighter than situation 2, showing a field polarity configuration as in Figure 4a. The antenna orientation in situation 1 is the same as that in situation 3. However, in this situation, the antenna is located in a much lower field strength region and its main emission is thus from its I-tip, as expected. All three situations are outlined in the right-most panels to illustrate the main electron emission maps.

D. Field strength, focal point imaging and pressure dependence

Our model for electron emission in Figure 4a and Figure 4b is based on the Fowler-Nordheim equation. To extract the value for the work function, we have taken a series of mode profile images at different incident THz field strengths. Experimentally, the incident THz pulses were variably attenuated by placing two wiregrid polarizers in the beam, and rotating the first one. For each image, we integrated the total light emission and used it for a Fowler-Nordhem plot. We find with an effective work function $\Phi = 0.9$ eV (see Supplementary Information for details). This value differs significantly from the commonly accepted value $\Phi = 5.1$ eV of the work function of Au in vacuum. An unusually low value for the effective work function at THz frequencies have been obserserved also in ambient THz-driven scanning tunneling microscopy (THz-STM) [3] and in THz-driven field emission from gold into a nitrogen (N_2) atmosphere [42]. The lowering of the effective work function is still a somewhat controversial observation, but it is appears reasonable that it originates from a combination of two effects, namely adsorbates and impurities on the gold surface and the surface topology of the gold. The interface is irregular on the sub-μm scale, and thus the field enhancement factor β calculated for a perfectly regular structure may locally be underestimated [3, 17, 42, 44]. There is good agreement between the observed light emission as function of THz field strength and the Fowler-Nordheim equation, which suggests that the electron-to-photon conversion is linear within the Ar glow discharge. The extracted work function is used in Figure 5a to plot the emission current density as a function of both the incident THz peak electric field and the corresponding field at the I-tip, including a 30% Fresnel loss at the backside of the substrate. We have scaled the experimental data accordingly (see Supplementary Information) to verify that we start to see light emission in the electron emission regime where tens of electrons are emitted. Considering that the vertical axis in Figure 5a covers 30 orders of magnitude within 4 orders in electric field, it is reassuring that our emission threshold is physically sensible. The experimentally determined threshold for detectable light emission is 55 kV/cm and the antenna at that point emits about 50 electrons/μm^2/ps.

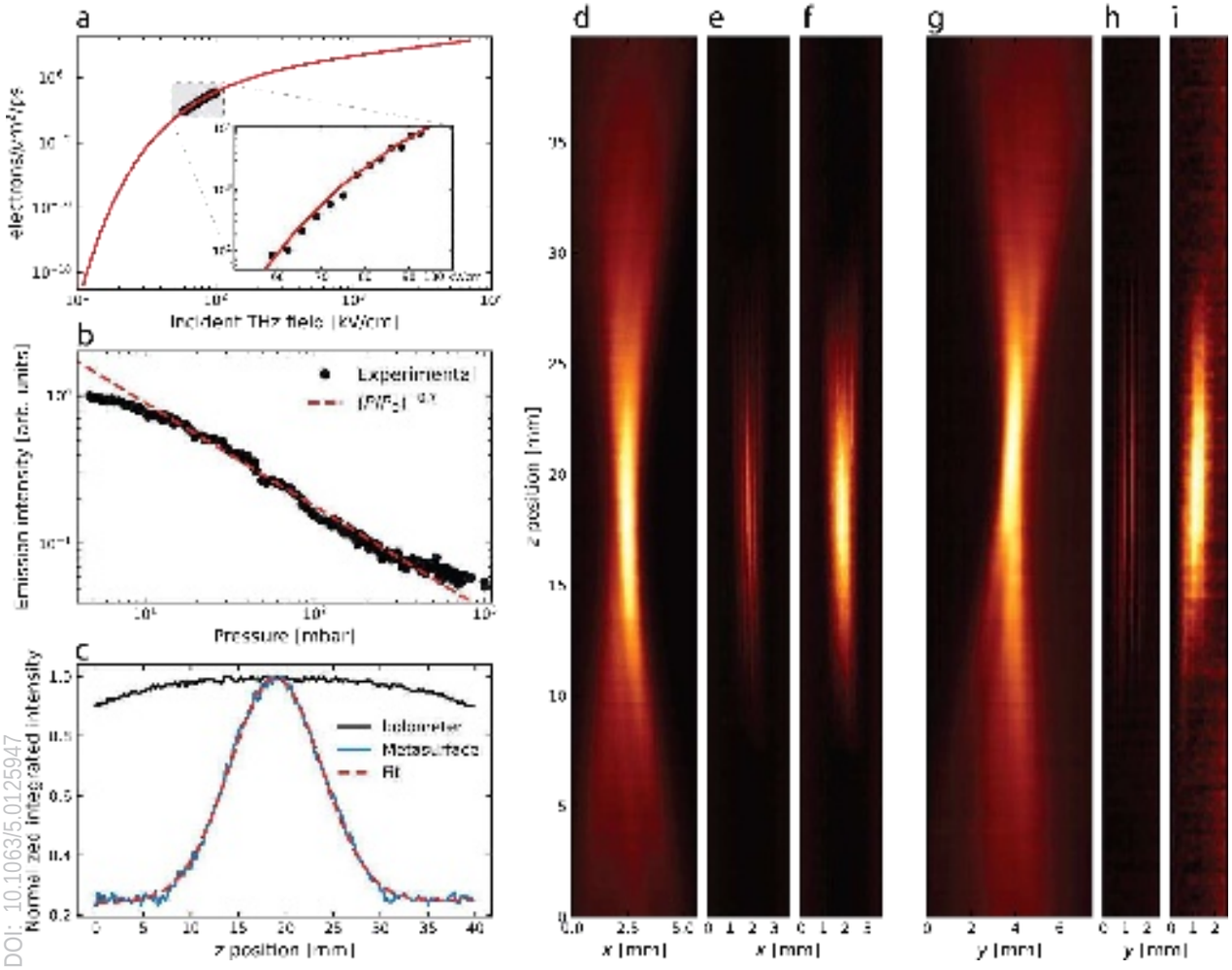

Figure 5: **Dependence of electron emission on incident THz peak field strength.** (a) The light emission from the Ar plasma glow discharge varies with the peak electric field strength according to the FN equation. (see Supplementary Information). Here, we used 100 kV/cm incident field, $\beta = 131.7$ and a Fresnel reflection at the substrate backside of 0.54. The main plot shows the FN emission curve in a large field range to illustrate the extreme nonlinearity of the tunneling process. The inset shows a close-up view of the data and the fit. The lower threshold for light emission is 55 kV/cm where we detect approximately 50 electrons /μm^2/ps. (b) Emission intensity at constant field strength as function of ambient gas pressure. The red, dashed curve is a phenomenological power-law dependence with an exponent of -0.7. (c) shows the integrated signal from the microbolometer camera (black curve) and the metasurface (blue curve) when scanned from the focal region of a focused THz beam. Dashed, red curve is a Guassian fit to the metasurface data. (d+g) horizontal (x) and vertical (y) projected intensity profile of the focused THz beam recorded by a microbolometer camera. (e+h) Projected light intensity profiles from the metasurface during the same scan range. (g+i) Binned versions of (e+h) (procedure is detailed in the Supplementary Information).

Figure 5b shows that the photon emission strength depends on the pressure of the surrounding argon gas in a nontrivial manner. Within the measured pressure range we see that at a few mbar pressure the light intensity is highest, and vanishes rapidly when the pressure is lowered below 1 mbar (not shown here). At higher pressures the light intensity decreases, approximately as $I \propto P^{-0.7}$ (dashed, blue curve in Figure 5b). As discussed in further detail in the Supplementary Information, we attribute this dynamics to the interplay between energy-dependent cross section for elastic electron scattering and excitation/ionization of the Ar atoms. Elastic scattering is most efficient at low energies and excitation/ionization is most efficient at higher energies [54].

Panels d-i in Figure 5 show a comparison between scanning a microbolometer camera (d+g) and our metasurface (e+h) through the focal point of a THz beam focused with an off-axis paraboloidal mirror with effective focal length of 50.8 mm (2”). Due to the discrete nature of the resonator array, the vertical lines Panels e+h represent a row or column of responators. To get a more comprehensive visualization of the beam profile, Panels f+i are binned versions of the metasurface data integrated over each period of the array (see Supplementary Information for further details). Panels d+e+f represent the projection of the beam profile onto the x (horizontal) axis, and Panels h+i+j represent the y (vertical) projection. All original cross-sectional images can be found in the Supplementary Information. The apparent cross section of the profile measured with the metasurface is comparable to that measured with the microbolometer camera. Due to the strongly nonlinear relation between THz field strength and emission strength a more narrow distribution is expected, so our observatrion is somewhat unexpected. However, we attribute this observation to several experimental factors. Firstly, the digital dynamic range of the CMOS camera images is 8 bits, so the limited dynamic range leads to a certain amount of saturation of the images (see Supplementary Information). A camera with higher bit depth would remove this artifact and lead to a more narrow apparent beam profile. Additionally, it is known that the microbolometer camera has better sensitivity at higher THz frequencies [55], and therefore tend to report a frequency-integrated beam profile of a broadband THz beam that is more narrow than the actual beam profile in the <1 THz frequency range where the metasurface has its highest sentivity in this experiment. Hence, a direct comparison of the beam profile widths makes little sense. More importantly, the beam profile comparison reveals that while the microbolometer camera records the beam profile across the full region, the metasurface only detects a signal in the narrow region near the focus where the peak field strength is highest. This is quantified in Figure 5c where the integrated signals along the z direction from the two cameras are compared. The microbolometer records the average power of the THz beam, which is independent of the focusing conditions, and hence the transversely integrated signal is approximately constant. The slight roll-off at the start end end of the range is due to the size of the beam profile exceeding that of the sensor array. In contrast, the metasurface records a signal only in the region close to the focal plane, with a FWHM of the response of less than 12 mm. Hence, the metasurface is well suited for efficient localization of the focal plane, even in a single-pixel version without imaging capabilities. The beam profile projections show that the focused THz beam has a certain amount of astigmatism in the form of different positions of the focal plane for the two projections. This astigmatism is reproduced in the metasurface images. It is worth noticing that given the fast response of the metasurface, it is possible to use it for single-shot THz imaging, as shown in the Supplementary Information.

Conclusions

In conclusion, we have demonstrated a new method for THz beam profiling that simultaneously measures the peak electric field and unambiguously determines the absolute polarity of single-cycle pulses. We use a

metasurface that enables lightwave-driven electron emission when excited with a short THz transient and subsequent light emission in the visible originating from an electron-induced local argon plasma discharge. Absolute calibration of incident peak electric field strength is possible for a given antenna structure and gas pressure. Further enhancements in sensitivity are expected by improvements in antenna design and tighter manufacturing tolerances. A significant advantage of our metasurface-based THz visualization method is its scalability and low fabrication costs; the size of the focal plane array can readily be increased to the full size of a standard wafer, and it can be fabricated by standard UV lithography and metal evaporation. This is in contrast to other THz beam profiling options, where the focal plane array typically is limited to a very small size, fabrication is expensive, and dedicated readout electronics is required.

We expect our approach to be broadly applicable to the far and mid-infrared spectral range by straightforward geometric scaling of the antenna dimensions. This indicates sensitivity across the THz and mid-IR ranges, although the sensitivity to absolute polarity becomes less relevant in the mid-IR, at least with current sources in this range that almost exclusively are limited to multi-cycle, symmetric pulse shapes. Finally, since our technique effectively uses up-conversion from the THz to the visible regime, standard silicon CMOS or CCD detectors can be uses for imaging, making it more cost effective than using a focal plane array designed to operate in the THz frequency range directly.

Supplementary material

See supplementary material for raw data for field dependence of electron emission, Fowler-Nordheim description of emission data, single-shot imaging, pressure dependence of the emission strength, alignment and saturation of the metasurface images, raw data for scans through the THz beam focus and a simulated sweep of the electrical conductivity for an antenna. In addition, a Particle-in-Cell simulation of the electron emission from an antenna can be found as a video file.

Acknowledgements

Use of the Linac Coherent Light Source, SLAC National Accelerator Laboratory, is supported by the US Department of Energy, Office of Science, Office of Basic Energy Sciences, under contract no. DE-AC02-76SF00515. M.C.H. is supported by the US Department of Energy, Office of Science, Office of Basic Energy Sciences, under award no. 2015-SLAC-100238-Funding. We also acknowledge funding from Independent Research Fund Denmark (ULTRA-TED).

References

[1] P. U. Jepsen, D. G. Cooke, and M. Koch, "Terahertz spectroscopy and imaging - Modern techniques and applications," Laser Photon. Rev. **5**, 124-166 (2011).

[2] T. Kampfrath, K. Tanaka, and K. A. Nelson, "Resonant and nonresonant control over matter and light by intense terahertz transients," Nat. Photon. **7**, 680-690 (2013).

[3] T. L. Cocker, V. Jelic, M. Gupta, S. J. Molesky, J. A. J. Burgess, G. D. L. Reyes, L. V. Titova, Y. Y. Tsui, M. R. Freeman, and F. A. Hegmann, "An ultrafast terahertz scanning tunnelling microscope," Nat. Photon. **7**, 620-625 (2013).

[4] B. C. Pein, W. Chang, H. Y. Hwang, J. Scherer, I. Coropceanu, X. Zhao, X. Zhang, V. Bulovic, M. Bawendi, and K. A. Nelson, "Terahertz-Driven Luminescence and Colossal Stark Effect in CdSe-CdS Colloidal Quantum Dots," Nano Lett **17**, 5375-5380 (2017).

[5] V. P. Wallace, E. MacPherson, J. A. Zeitler, and C. Reid, "Three-dimensional imaging of optically opaque materials using nonionizing terahertz radiation," J. Opt. Soc. Am. A-Opt. Image Sci. Vis. **25**, 3120-3133 (2008).

[6] C. Kealhofer, W. Schneider, D. Ehberger, A. Ryabov, F. Krausz, and P. Baum, "All-optical control and metrology of electron pulses," Science **352**, 429-433 (2016).

[7] K. Yoshioka, I. Katayama, Y. Minami, M. Kitajima, S. Yoshida, H. Shigekawa, and J. Takeda, "Real-space coherent manipulation of electrons in a single tunnel junction by single-cycle terahertz electric fields," Nat. Photonics **10**, 762-765 (2016).

[8] A. T. Tarekegne, B. Zhou, K. Kaltenecker, K. Iwaszczuk, S. Clark, and P. U. Jepsen, "Terahertz time-domain spectroscopy of zone-folded acoustic phonons in 4H and 6H silicon carbide," Opt Express **27**, 3618-3628 (2019).

[9] P. Planken, "MICROSCOPY A terahertz nanoscope," Nature **456**, 454-455 (2008).

[10] C. Yu, S. Fan, Y. Sun, and E. Pickwell-Macpherson, "The potential of terahertz imaging for cancer diagnosis: A review of investigations to date," Quant Imaging Med Surg **2**, 33-45 (2012).

[11] C. L. K. Dandolo, and P. U. Jepsen, "Wall Painting Investigation by Means of Non-invasive Terahertz Time-Domain Imaging (THz-TDI): Inspection of Subsurface Structures Buried in Historical Plasters," J. Infrared Millim. Terahertz Waves **37**, 198-208 (2016).

[12] A. G. Davies, A. D. Burnett, W. H. Fan, E. H. Linfield, and J. E. Cunningham, "Terahertz spectroscopy of explosives and drugs," Mater. Today **11**, 18-26 (2008).

[13] P. L. Kramer, M. K. R. Windeler, K. Mecseki, E. G. Champenois, M. C. Hoffmann, and F. Tavella, "Enabling high repetition rate nonlinear THz science with a kilowatt-class sub-100 fs laser source," Opt. Express **28**, 16951-16967 (2020).

[14] J. A. Fülöp, S. Tzortzakis, and T. Kampfrath, "Laser-Driven Strong-Field Terahertz Sources," Advanced Optical Materials **8**, 1900681 (2020).

[15] V. A. Andreeva, O. G. Kosareva, N. A. Panov, D. E. Shipilo, P. M. Solyankin, M. N. Esaulkov, P. Gonzalez de Alaiza Martinez, A. P. Shkurinov, V. A. Makarov, L. Berge, and S. L. Chin, "Ultrabroad Terahertz Spectrum Generation from an Air-Based Filament Plasma," Phys Rev Lett **116**, 063902 (2016).

[16] A. Houard, Y. Liu, B. Prade, V. T. Tikhonchuk, and A. Mysyrowicz, "Strong enhancement of terahertz radiation from laser filaments in air by a static electric field," Phys Rev Lett **100**, 255006 (2008).

[17] K. Iwaszczuk, M. Zalkovskij, A. C. Strikwerda, and P. U. Jepsen, "Nitrogen plasma formation through terahertz-induced ultrafast electron field emission," Optica **2** (2015).

[18] G. Herink, L. Wimmer, and C. Ropers, "Field emission at terahertz frequencies: AC-tunneling and ultrafast carrier dynamics," New Journal of Physics **16** (2014).

[19] S. L. Lange, N. K. Noori, T. M. B. Kristensen, K. Steenberg, and P. U. Jepsen, "Ultrafast THz-driven electron emission from metal metasurfaces," Journal of Applied Physics **128** (2020).

[20] O. Schubert, M. Hohenleutner, F. Langer, B. Urbanek, C. Lange, U. Huttner, D. Golde, T. Meier, M. Kira, S. W. Koch, and R. Huber, "Sub-cycle control of terahertz high-harmonic generation by dynamical Bloch oscillations," Nat. Photon. **8**, 119-123 (2014).

[21] D. Golde, T. Meier, and S. W. Koch, "High harmonics generated in semiconductor nanostructures by the coupled dynamics of optical inter- and intraband excitations," Physical Review B **77**, 6 (2008).

[22] M. C. Hoffmann, and D. Turchinovich, "Semiconductor saturable absorbers for ultrafast terahertz signals," Appl. Phys. Lett. **96**, 151110 (2010).

[23] E. Goulielmakis, V. S. Yakovlev, A. L. Cavalieri, M. Uiberacker, V. Pervak, A. Apolonski, R. Kienberger, U. Kleineberg, and F. Krausz, "Attosecond Control and Measurement: Lightwave Electronics," Science **317**, 769-775 (2007).

[24] F. Langer, M. Hohenleutner, C. P. Schmid, C. Poellmann, P. Nagler, T. Korn, C. Schüller, M. S. Sherwin, U. Huttner, J. T. Steiner, S. W. Koch, M. Kira, and R. Huber, "Lightwave-driven quasiparticle collisions on a subcycle timescale," Nature **533**, 225-229 (2016).

[25] S. S. Dhillon, M. S. Vitiello, E. H. Linfield, A. G. Davies, C. H. Matthias, B. John, P. Claudio, M. Gensch, P. Weightman, G. P. Williams, E. Castro-Camus, D. R. S. Cumming, F. Simoens, I. Escorcia-Carranza, J. Grant, L. Stepan, K.-G. Makoto, K. Kuniaki, K. Martin, A. S. Charles, L. C. Tyler, H. Rupert, A. G. Markelz, Z. D. Taylor, P. W. Vincent, J. A. Zeitler, S. Juraj, M. K. Timothy, B. Ellison, S. Rea, P. Goldsmith, B. C. Ken, A. Roger, D. Pardo, P. G. Huggard, V. Krozer, S. Haymen, F. Martyn, R. Cyril, S. Alwyn, S. Andreas, N. Mira, R. Nick, C. Roland, E. C. John, and B. J. Michael, "The 2017 terahertz science and technology roadmap," J. Phys. D **50**, 043001 (2017).

[26] Q. Wu, and X. C. Zhang, "FREE-SPACE ELECTROOPTIC SAMPLING OF TERAHERTZ BEAMS," Applied Physics Letters **67**, 3523-3525 (1995).

[27] T. W. Wang, K. Iwaszczuk, E. A. Wrisberg, E. V. Denning, and P. U. Jepsen, "Linearity of Air-Biased Coherent Detection for Terahertz Time-Domain Spectroscopy," J. Infrared Millim. Terahertz Waves **37**, 592-604 (2016).

[28] Q. Wu, T. D. Hewitt, and X. C. Zhang, "Two-dimensional electro-optic imaging of THz beams," Appl. Phys. Lett. **69**, 1026-1028 (1996).

[29] T. S. Hartwick, D. T. Hodges, D. H. Barker, and F. B. Foote, "Far infrared imagery," Appl. Opt. **15**, 1919-1922 (1976).

[30] Q. Li, S.-H. Ding, R. Yao, and Q. Wang, "Real-time terahertz scanning imaging by use of a pyroelectric array camera and image denoising," J. Opt. Soc. Am. A **27**, 2381-2386 (2010).

[31] A. W. Lee, and Q. Hu, "Real-time, continuous-wave terahertz imaging by use of a microbolometer focal-plane array," Opt. Lett. **30**, 2563-2565 (2005).

[32] N. Oda, "Uncooled bolometer-type Terahertz focal plane array and camera for real-time imaging," Comptes Rendus Physique **11**, 496-509 (2010).

[33] I. Kasalynas, A. J. L. Adam, T. O. Klaassen, J. N. Hovenier, G. Pandraud, V. P. Iordanov, and P. M. Sarro, "Design and performance of a room-temperature terahertz detection array for real-time imaging," IEEE Journal of Selected Topics in Quantum Electronics **14**, 363-369 (2008).

[34] S. L. Lange, T. M. B. Kristensen, K. Iwaszczuk, and P. U. Jepsen, "Space-Time mapping of terahertz-induced electron field emission," in *2017 42nd International Conference on Infrared, Millimeter, and Terahertz Waves (IRMMW-THz)*(2017).

[35] A. T. Tarekegne, K. Iwaszczuk, M. Zalkovskij, A. C. Strikwerda, and P. U. Jepsen, "Impact ionization in high resistivity silicon induced by an intense terahertz field enhanced by an antenna array," New Journal of Physics **17**, 9 (2015).

[36] S.-D. Liang, *Quantum Tunneling and Field Emission Theories* (World Scientific, 2014).

[37] A. Bogaerts, R. Gijbels, and J. Vlcek, "Collisional-radiative model for an argon glow discharge," Journal of Applied Physics **84**, 121-136 (1998).

[38] A. Bogaerts, R. Gijbels, and J. Vlcek, "Modeling of glow discharge optical emission spectrometry: Calculation of the argon atomic optical emission spectrum," Spectroc. Acta Pt. B-Atom. Spectr. **53**, 1517-1526 (1998).

[39] A. C. Strikwerda, M. Zalkovskij, K. Iwaszczuk, D. L. Lorenzen, and P. U. Jepsen, "Permanently reconfigured metamaterials due to terahertz induced mass transfer of gold," Opt Express **23**, 11586-11599 (2015).

[40] K. Iwaszczuk, R. Malureanu, M. Zalkovskij, A. C. Strikwerda, and P. U. Jepsen, "Terahertz-field-induced photoluminescence of nanostructured gold films," in *2013 38th International Conference on Infrared, Millimeter, and Terahertz Waves (IRMMW-THz)*(2013), pp. 1-1.

[41] A. Abramovich, N. S. Kopeika, D. Rozban, and E. Farber, "Inexpensive detector for terahertz imaging," Appl. Optics **46**, 7207-7211 (2007).

[42] K. Iwaszczuk, M. Zalkovskij, A. C. Strikwerda, and P. U. Jepsen, "Nitrogen plasma formation through terahertz-induced ultrafast electron field emission," Optica **2**, 116-123 (2015).

[43] J. Zhang, X. Zhao, K. Fan, X. Wang, G.-F. Zhang, K. Geng, X. Zhang, and R. D. Averitt, "Terahertz radiation-induced sub-cycle field electron emission across a split-gap dipole antenna," Appl. Phys. Lett. **107**, 231101 (2015).

[44] T. L. Cocker, V. Jelic, M. Gupta, S. J. Molesky, J. A. J. Burgess, G. De Los Reyes, L. V. Titova, Y. Y. Tsui, M. R. Freeman, and F. A. Hegmann, "An ultrafast terahertz scanning tunnelling microscope," Nat. Photonics **7**, 620-625 (2013).

[45] T. Rybka, M. Ludwig, M. F. Schmalz, V. Knittel, D. Brida, and A. Leitenstorfer, "Sub-cycle optical phase control of nanotunnelling in the single-electron regime," Nat. Photonics **10**, 667-670 (2016).

[46] P. Klarskov, A. T. Tarekegne, K. Iwaszczuk, X. C. Zhang, and P. U. Jepsen, "Amplification of resonant field enhancement by plasmonic lattice coupling in metallic slit arrays," Sci Rep **6**, 37738 (2016).

[47] S. Bagiante, F. Enderli, J. Fabianska, H. Sigg, and T. Feurer, "Giant electric field enhancement in split ring resonators featuring nanometer-sized gaps," Sci Rep **5**, 8051 (2015).

[48] J.-H. Kang, D.-S. Kim, and M. Seo, "Terahertz wave interaction with metallic nanostructures," Nanophotonics **7**, 763-793 (2018).

[49] K.-L. Yeh, M. C. Hoffmann, J. Hebling, and K. A. Nelson, "Generation of 10μJ ultrashort terahertz pulses by optical rectification," Applied Physics Letters **90**, 171121 (2007).

[50] J. Hebling, G. Almasi, I. Z. Kozma, and J. Kuhl, "Velocity matching by pulse front tilting for large-area THz-pulse generation," Opt. Express **10**, 1161-1166 (2002).

[51] P. U. Jepsen, C. Winnewisser, M. Schall, V. Schyja, S. R. Keiding, and H. Helm, "Detection of THz pulses by phase retardation in lithium tantalate," Phys. Rev. E **53**, R3052-R3054 (1996).

[52] Q. Wu, and X. C. Zhang, "Free-space electro-optic sampling of terahertz beams," Appl. Phys. Lett. **67**, 3523-3525 (1995).

[53] A. Bitzer, J. Wallauer, H. Merbold, H. Helm, T. Feurer, and M. Walther, "Lattice modes mediate radiative coupling in metamaterial arrays," Opt. Express **17**, 22108-22113 (2009).

[54] G. G. Raju, "Electron-atom collision cross sections in argon: an analysis and comments," IEEE Transactions on Dielectrics and Electrical Insulation **11**, 649-673 (2004).

[55] N. Oda, "Uncooled bolometer-type terahertz focal plane array and camera for real-time imaging," C. R. Phys. **11**, 496–509 (2010).

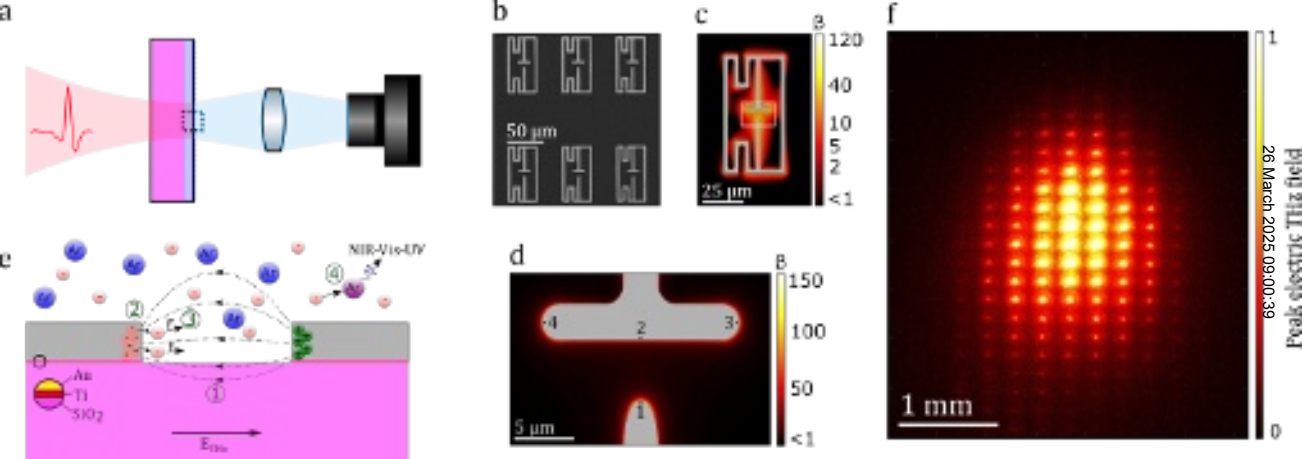
a
b
50 μm
c
B
120
40
10
5
2
<1
25 μm
d
B
150
100
50
<1
5 μm
1
2
3
4
e
NIR-Vis-UV
Au
Ti
SiO2
f
1 mm
1
0
Peak electric field
26 March 2025 09:00:39

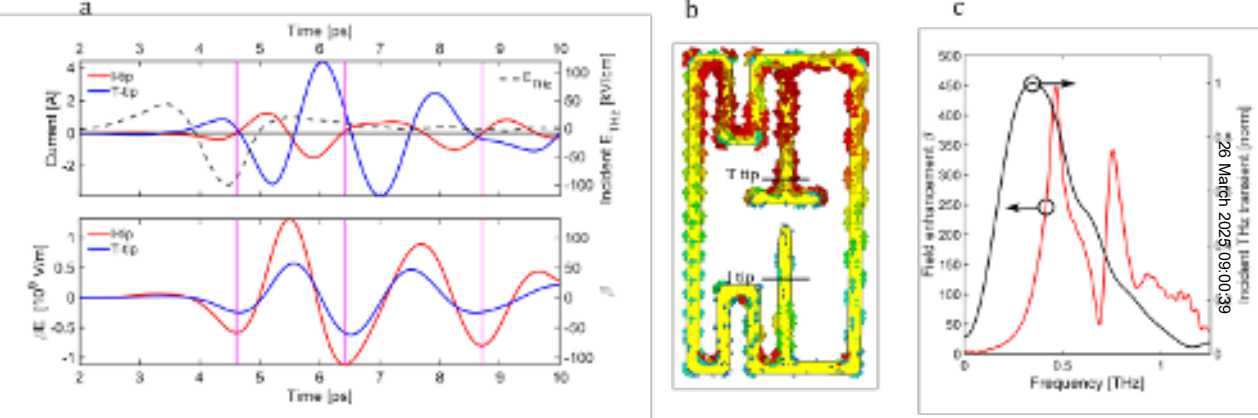
a
b
c
Time [ps]
Current [A]
Incident E_{THz} [KV/cm]
ΔE [10^6 V/m]
Time [ps]
S-tip
T-tip
E_{inc}
S tip
T tip
Field enhancement
Incident THz transient (norm)
Frequency [THz]
26 March 2025 09:00:39

3 µm

27 µm

15 µm

40 µm

26 March 2025 09:00:39

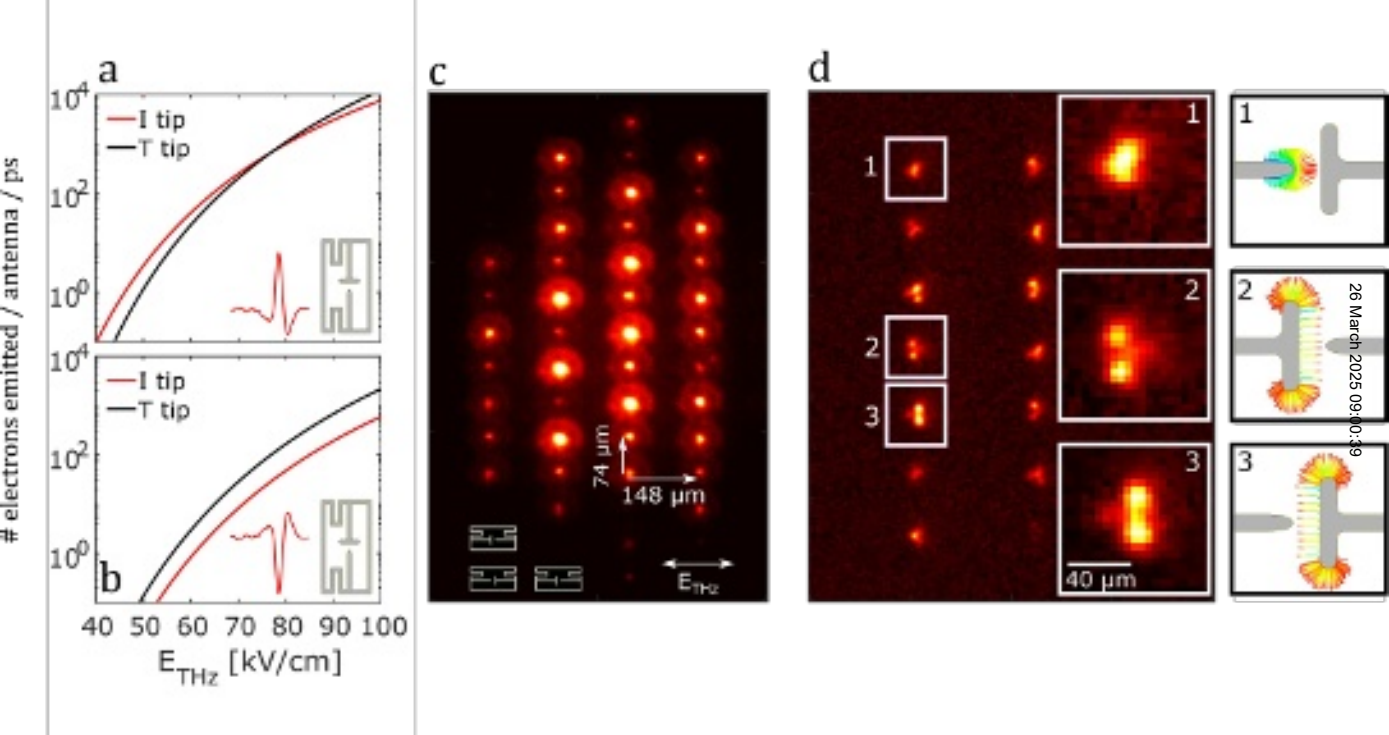

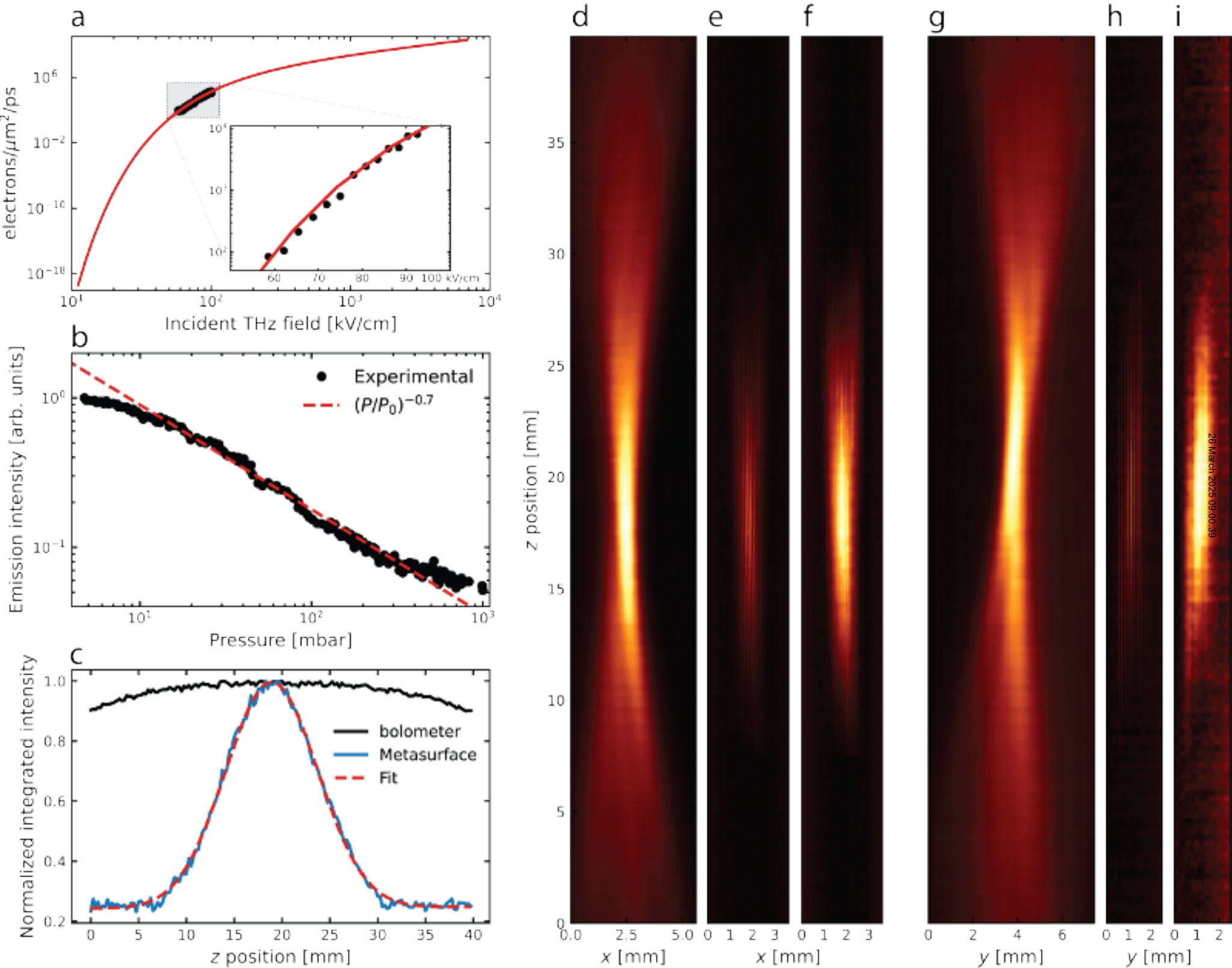
a
electrons/μm²/ps
Incident THz field [kV/cm]
60 70 80 90 100 kV/cm
b
Emission intensity [arb. units]
Experimental
(P/P0)^−0.7
Pressure [mbar]
c
Normalized integrated intensity
bolometer
Metasurface
Fit
z position [mm]
d
e
f
g
h
i
z position [mm]
x [mm]
x [mm]
y [mm]
y [mm]
26 March 2025 09:00:39